Ultramicroscopy 248 (2023) 113715

Contents lists available at ScienceDirect

Ultramicroscopy

journal homepage: www.elsevier.com/locate/ultramic

Correcting for probe wandering by precession path segmentation

Gregory Nordahl [a,*], Lewys Jones [b,c], Emil Frang Christiansen [a], Kasper Aas Hunnestad [d], Magnus Nord [a]

[a] Department of Physics, Norwegian University of Science and Technology (NTNU), 7491 Trondheim, Norway
[b] School of Physics, Trinity College Dublin, Dublin 2, Ireland
[c] Advanced Microscopy Laboratory, Centre for Research on Adaptive Nanostructures and Nanodevices (CRANN), Dublin 2, Ireland
[d] Department of Materials Science and Engineering, Norwegian University of Science and Technology (NTNU), 7491 Trondheim, Norway

ARTICLE INFO

Dataset link: https://zenodo.org/record/7702229

Keywords:
Electron diffraction
Precession
Aberrations
Alignment

ABSTRACT

Precession electron diffraction has in the past few decades become a powerful technique for structure solving, strain analysis, and orientation mapping, to name a few. One of the benefits of precessing the electron beam, is increased reciprocal space resolution, albeit at a loss of spatial resolution due to an effect referred to as 'probe wandering'. Here, a new methodology of precession path segmentation is presented to counteract this effect and increase the resolution in reconstructed virtual images from scanning precession electron diffraction data. By utilizing fast pixelated electron detector technology, multiple frames are recorded for each azimuthal rotation of the beam, allowing for the probe wandering to be corrected in post-acquisition processing. Not only is there an apparent increase in the resolution of the reconstructed images, but probe wandering due to instrument misalignment is reduced, potentially easing an already difficult alignment procedure.

1. Introduction

Ever since the concept of precession electron diffraction (PED) was introduced by Vincent and Midgley almost 30 years ago [1], the technique has seen an increase in popularity owing to the benefits of electron beam precession. Today it is an invaluable tool for structure determination [2–4], strain measurements [5], and phase- and orientation mapping [6,7]. Precessing the beam equates to the Ewald sphere sampling a volume of reciprocal space [8], exciting more reflections than conventional electron diffraction. At the same time, the individual reflection intensities appear kinematic-like [9,10], with a monotonic intensity increase over a large thickness range with little variation between equally excited reflections [11].

Although precession leads to an increased angular resolution in reciprocal space [12], experimental limitations mean that the spatial resolution suffers increasingly with higher precession angles; this is apparent in virtual bright field (VBF) reconstructions from scanning PED (SPED) data performed by Barnard et al. (2017) [13]. Due to the off-axis tilt of the beam, the probe is traversing the aberration surface in a circular pattern during precession, being displaced from the optical axis by a shift equal to the local gradient of the aberration function at each point on the precession azimuth [8]. These shifts will lead to an increased time averaged and effective probe size. The probe shifts, often referred to as 'probe wandering' due to the periodic nature of the motion, are dominated by the unavoidable spherical aberration of the probe forming lens even under perfect alignment conditions [14]. However, PED alignment is known to be difficult and a lot of research has gone into optimizing the procedure [5,8,12,13]. In a well aligned PED setup, the beam crossover and precession pivot point are both perfectly coincident on the sample surface [13]. A deviation of either would induce the same probe wandering as mentioned earlier, likely with a greater contribution than from spherical aberration. Although probe wandering is inherent to PED, the motion is periodic and, as will be shown, has the potential to be corrected.

A useful application of SPED data is virtual imaging [15]. By integrating the intensity within a virtual aperture placed in the detector plane of the 4D dataset, an intensity map as a function of probe position can be constructed [16]. The virtual aperture can be placed to create virtual images corresponding to bright field-, dark-field-, annular dark-field images and more, making it a very versatile tool. The application of precession means the virtual image is a 2D map of the integrated rocking curve of the chosen reflection [1]. Since this integration shows less dynamical effects, especially in terms of bending and thickness variations [17], the virtual image becomes more easily interpretable in terms of diffraction conditions. In this work we present the methodology of precession path segmentation to counteract probe wandering, reducing precession-induced blur which leads to a

* Corresponding author.
E-mail address: gregory.nordahl@ntnu.no (G. Nordahl).

https://doi.org/10.1016/j.ultramic.2023.113715
Received 21 November 2022; Received in revised form 22 February 2023; Accepted 2 March 2023
Available online 8 March 2023

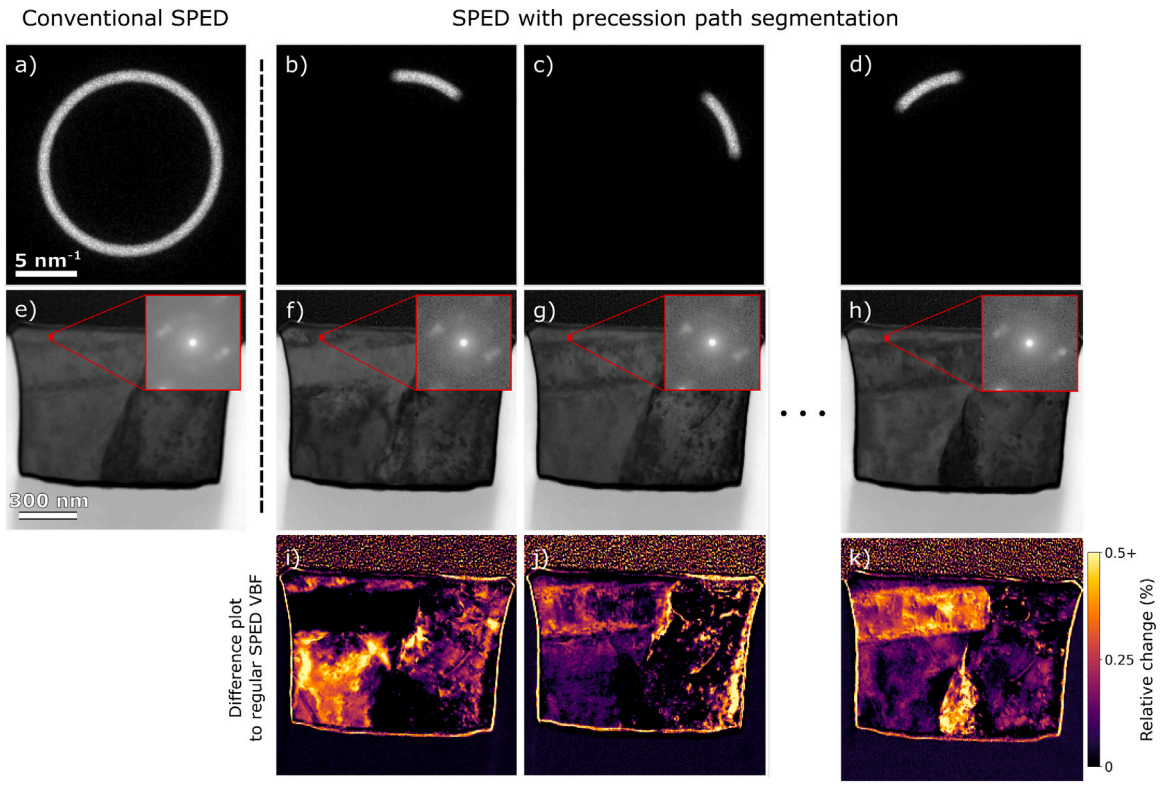

Fig. 1. A comparison between a regular SPED scan, and a precession path segmented SPED scan with $n = 8$ segments. Example of diffraction patterns with de-rocking switched off for (a) the regular SPED scan, and (b)–(d) three precession path segments. VBF images of a (e) regular SPED scan, and (f)–(h) three segments. Insets show diffraction patterns for 4 × 4 selected scan points in the VBF images. VBF intensity difference plots between each of the presented segment VBF images in (f)–(h) compared to the regular SPED VBF in (e) are shown in (i)–(k). The diffraction patterns in (a)–(d) are from a different precession path segmentation scan than the VBF images and difference plots in (e)–(k).

loss of spatial resolution in virtual images reconstructed from SPED scans [13]. The basis of this methodology lies in fast pixelated detector technology, as the goal is to record several frames in quick succession for each azimuthal rotation of the beam. Results are presented from two applications of the methodology, one on a regular, well-aligned SPED scan, and one where a precession misalignment has been introduced to demonstrate the capabilities of the technique.

2. Experimental methods

To perform precession path segmentation, the first step is to align the instrument for SPED acquisition. These experiments were carried out on a JEOL JEM-2100F operating at 200 kV, equipped with a NanoMEGAS DigiSTAR precession scan generator and a Quantum Detectors single chip MerlinEM direct electron detector. The SPED alignment was done by following the double-rocking alignment outlined by Barnard et al. (2017) [13], applied on a nanobeam diffraction 1 nm probe with a 1.2 mrad convergence semi-angle. The precession angle was set to 1.0°, or approximately 17.5 mrad, and the precession frequency to 100 Hz. The selected precession angle is expected to bring the beam out of the aberration free area for such a non-corrected instrument.

After the alignment, scans were set up to record precession path segmentation datasets with $n = 8$ segments, meaning that the detector had to record 8 frames at each scan position. With the selected precession frequency, the dwell time was set to 10 ms to allow the beam one full rotation around the optical axis, and the scanner frame points were set to 256 × 256. Consequently, the detector capture time was set to 10/8 ms = 1.25 ms, and frame captures to 2048 × 256. In other words, the capture time was $1/n$ of the dwell time, and the number of frames per scan line recorded was multiplied by n. To allow this increased amount of data to be recorded by the detector, the scanner flyback parameter had to be increased by a significant amount. The resulting dataset ends up being n times larger than a regular SPED scan, and typically 2–3 times slower in recording, however during the flyback time the beam is off away to the side and adds minimal beam-damage to the region of interest. The number of segments was chosen so that diffraction patterns in each segment contained sufficient intensity for VBF reconstruction. To increase the amount of segments while maintaining adequate intensity levels in diffraction patterns, the precession frequency could be reduced.

Two SPED scans were recorded with our proposed precession path segmentation employed. One scan had a scan step size of 5.6 nm and was performed with a proper precession alignment, while the other had a scan step size of 10.2 nm and an intentional precession pivot point misalignment. The intentional misalignment was performed by adjusting X and Y scan coil amplitudes equally by 0.1% to offset the proper alignment. These intentionally lightly misaligned datasets serve as extreme tests of what might be a reasonable worst-case scenario with an experienced operator. The large 4D-STEM datasets were processed with the open-source Python libraries HyperSpy [18] and pyxem [19]. Initially, the 2048 × 256 dataset is sliced into 8 pieces, each of 256 × 256 scan dimensions. From these slices, VBF reconstructions are created. Since probe wandering is equal at every scan point within a given precession angle, the features in the synthesized VBF images move relative to each other in a circular motion. This movement is corrected for by inserting the images as a stack into the SmartAlign plugin for Gatan Microscopy Suite, and performing rigid correction [20] between the VBF images. Rigid correction works to offset the translation between the images in the stack by correlation functions calculated in Fourier space. The scans were correlated with the phase correlation function on selected region of interests that include visibly traceable feature edges surrounded by amorphous regions. Before rigid correction is performed, SmartAlign upscales the inserted images by a factor of two, which is

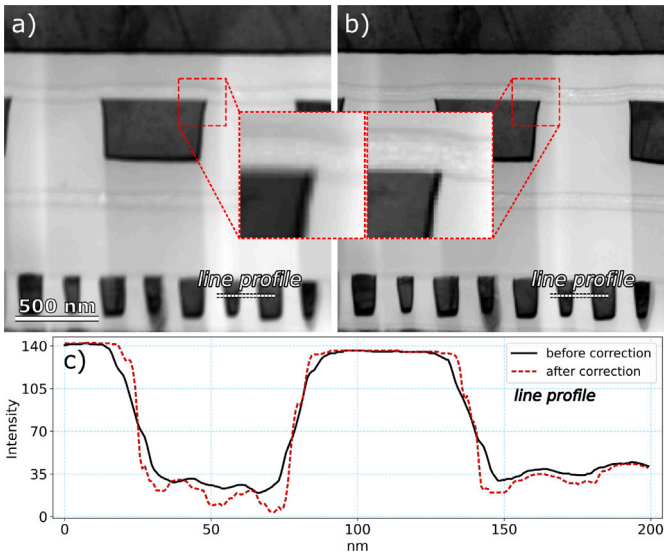

Fig. 2. VBF images from a precession path segmented SPED scan where an intentional pivot point misalignment has been introduced, showing the sums (a) before and (b) after rigid correction. (c) Line profiles from the same region in both scans are included.

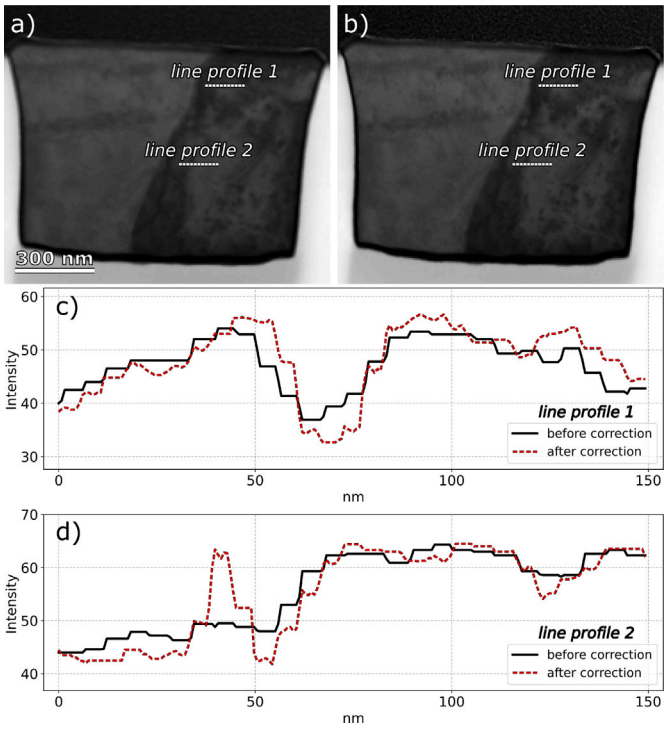

Fig. 3. VBF images from a precession path segmented SPED scan with a proper alignment. Sum of individual VBF (a) before and (b) after rigid correction. (c) and (d) Intensity profiles from two different regions have been extracted from the two VBF sums.

possible due to the fact that the scan step sizes are much larger than the probe size. As a final step, the corrected images are summed to get a single 256 × 256 VBF image output, and compared to a non-corrected VBF image sum. The non-corrected VBF image sum is equivalent to a conventional, non-segmented SPED scan VBF reconstruction (see Supplementary Material).

Fig. 1 illustrates the concept of precession path segmentation with $n = 8$ segments. In conventional PED or SPED, the detector integrates the intensity in the diffraction plane for an integer number of beam rotations around the optical axis. Fig. 1(a) illustrates the precession path in a diffraction pattern with de-rocking switched off, which is a projection of the hollow-cone SPED beam illumination. By capturing an integer number of frames per rotation of the beam around the optical axis, the integration regions become smaller. Three of in total eight intensity integration regions can be seen in the non-de-rocked diffraction patterns in Fig. 1(b)–(d).

The methodology was tested on a focused ion beam (FIB) cross-section lift-out of the integrated circuitry of a central processing unit (CPU) chip. VBF images were reconstructed from the regular SPED scan in Fig. 1(e), and from three segments of the precession path segmentation dataset in Fig. 1(f)–(h). Inset axes show average diffraction patterns extracted from 4 × 4 pixel positions, due to limited individual diffraction pattern intensities. Difference in intensity plots have been created comparing the different VBF segments to the conventional SPED VBF, as seen in Fig. 1(i)–(k). The scans were of large crystalline feature surrounded by amorphous areas and a polycrystalline FIB deposited Pt layer. Notice that, in the difference plots, the largest changes in intensity between individual segment VBF and regular SPED VBF are happening in the crystalline region. In a segment of the precession path, not only is the angular integration of the beam different, but also the segment's probe wandering will be a fraction of that for the full precession path. The apparent change in diffraction contrast reflects these two contributions.

3. Results and discussion

The VBF images from the precession path segmented scan with a larger step size can be seen in Fig. 2, before and after rigid correction performed in SmartAlign. As previously mentioned, the scan had a small intentional pivot point misalignment introduced, and the probe shifts were estimated to be up to 13 nm from the scan point center based on feature movement. The misalignment leads to blur in the VBF image when summed without correction, while the rigid corrected VBF image shows a noticeable increase in resolution. The relative blurring is equivalent to the rigid corrected VBF image being convoluted with a Gaussian kernel 3 px in size with a standard deviation of $\sigma = 7$. An intensity profile was extracted from equal positions in both images, covering a region with two crystalline features. The features show a larger dynamic range of intensity values and much higher structural variations in the rigidly corrected image as compared to the non-corrected one. The transition between a crystalline feature and the surrounding amorphous regions, i.e. the edges of the features, are also sharper. Least squares curve fitting was performed to estimate the increase in edge steepness between the uncorrected and corrected VBF images. An arctangent function, $A \cdot \arctan\left[k\left(x - x_0\right)\right]$ with fitting parameters $A, k,$ and x_0, was fit on the rising edge of the feature as seen in the line profile between 70 nm and 90 nm. Results of the curve fittings had slope parameters, k, of 0.15 ± 0.01 for the non-corrected VBF edge, and 0.38 ± 0.03 for the corrected one, in other words a 2.5 times increase in edge steepness.

A comparison of VBF images before and after rigid correction, from the precession path segmented scan with a smaller step size, can be seen in Fig. 3. As the scan did not have an intentional pivot point misalignment introduced as the previous one, visually there is a small, but noticeable, difference between the before- and after corrected images. Here the probe shifts have been estimated to be up to 7 nm. Two intensity profiles have been extracted from equal positions in both images, as seen in Fig. 3 (b) and (c). The intensity range in these profiles are on a much smaller scale than the profile in Fig. 2(c), allowing us to see the small structural variations inside the crystalline region.

The first profile covers a region with a small feature as seen by the dip in intensity centered around the 70 nm point. The feature appears to have sharper edges and a larger range of intensity values in the corrected image in comparison to the non-corrected one. In

the second profile, an intensity spike around the 40 nm point appears in the corrected image which is not seen in the non-corrected one. Both profiles hint at increased resolution after rigid correction, while the non-corrected VBF image appears more blurred due to the probe wandering.

The experimental results above show that the resolution can be increased in VBF images when probe wandering of 7 nm to 13 nm is present. Although the scan that showed the smallest wandering was aligned to the best extent of the operator, it is difficult to state to what degree the spherical aberration of the probe forming lens influences the shifts. It has been reported that shifts down to 1 nm are possible for an aberration corrected instrument [8], which would imply that the 7 nm shifts observed in the non-corrected instrument are to a large degree influenced by the spherical aberration. Probe wandering may occur within individual precession path segments, e.g., if the beam experiences a steep change in the aberration function due to a non-circular precession path. However, this does not need to apply for all the segments, and so those that experience large probe shifts can be selectively discarded. This would effectively create a SPED scan with a percentage of the full precession path.

To achieve the most precise results with this technique, with the highest freedom to select which segments would contribute to the final compound SPED scan, the precession path should be segmented until each segment resembles a single probe. For a probe with semi-convergence angle, $\alpha = 1.2$ mrad and with a precession angle $\phi = 17.5$ mrad, to achieve single-probe segments one would have to segment the scan $2\pi\phi/2\alpha \approx 46$ times. This would drastically increase the scan size, and each individual segment's diffraction patterns would have very low intensity unless compensated for by having a much smaller precession frequency than the 100 Hz utilized. The final result would imitate a ϕ-tilt series, albeit being recorded instantaneously with all information present in one single scan. It is worth pointing out that although precession path segmentation increases the apparent resolution in VBF images, it does so by counteracting the effect of probe wandering from the beam precessing on an aberration surface. The optimum case, as described above, will be achieved with a segmented scan where each segment of intensity integration takes the appearance of a single beam, but the resolution will not be increased further than what is achievable without precession.

The methodology in this article has been applied solely to VBF reconstructions, since probe wandering is straightforward recognizable as feature movement between the images corresponding to different segments of the precession path. However, it is also possible to correct for probe wandering by overlapping diffraction patterns from different segments that correspond to the same spatial position of the probe. Since probe wandering is present, the individual segments of the scan need to be shifted by a fixed amount in both spatial directions. The shifts can be estimated based on first performing VBF reconstructions and measuring the displacement of recognizable features between the different VBF images, as done previously. More optimally one could calculate the shifts based on experimental parameters and the aberrations of the probe forming lens [8], and attempt to match probe step size in the scan for accurate fitting. This is a challenge as one would essentially attempt to reconstruct a circular path using a finite amount of pixels, which would work for horizontal and vertical pixels, albeit not diagonal elements. To better fit the distance between pixels on a diagonal, one could set up a scan with a step size a fraction of the expected probe shifts.

4. Conclusion

To conclude, we have presented a methodology to increase the resolution in VBF images from SPED data by reducing the effect of probe wandering, a by-product of electron beam precession which causes image blur. By segmenting the precession path, and performing VBF reconstructions on individual segments, apparent feature movement between images stemming from probe shifts is rigidly corrected in SmartAlign. The final output, which is a sum of the rigidly corrected VBF images, shows a significant reduction in blur, particularly evident in the small structural elements that appeared after correction. The methodology has proven effective in correcting the shifts due to instrumental misalignment, which might help to ease the alignment procedure for the operator, or alternatively, allow for more throughput on a microscopy session as the alignment requirements are less strict for high quality imaging.

Declaration of competing interest

The authors declare that they have no known competing financial interests or personal relationships that could have appeared to influence the work reported in this paper.

Data availability

All original datasets, with scripts to process these and to process the images after SmartAlign correction, can be found at https://zenodo.org/record/7702229.

Acknowledgments

We wish to acknowledge the support from the Research Council of Norway for the Norwegian Center for Transmission Electron Microscopy, NORTEM (197405), the Norwegian Micro- and Nano-Fabrication Facility, NorFab (295864), and In-situ Correlated Nanoscale Imaging of Magnetic Fields in Functional Materials, InCoMa (315475). LJ acknowledges funding from Science Foundation Ireland grant URF/RI/191637. We would also like to thank Dr. Tina Bergh at NTNU for recording the dataset to visualize the technique, and Colin Kirkbride at the University of Glasgow for helping with visual design.

Appendix A. Supplementary data

Supplementary material related to this article can be found online at https://doi.org/10.1016/j.ultramic.2023.113715.

References

[1] R. Vincent, P. Midgley, Double conical beam-rocking system for measurement of integrated electron diffraction intensities, Ultramicroscopy 53 (3) (1994) 271–282, http://dx.doi.org/10.1016/0304-3991(94)90039-6.

[2] D. Xie, C. Baerlocher, L.B. McCusker, Combining precession electron diffraction data with X-ray powder diffraction data to facilitate structure solution, J. Appl. Crystallogr. 41 (6) (2008) 1115–1121, http://dx.doi.org/10.1107/S0021889808034377.

[3] T.A. White, M.S. Moreno, P.A. Midgley, Structure determination of the intermediate tin oxide Sn3O4 by precession electron diffraction, Z. Kristallogr. 225 (2–3) (2010) 56–66, http://dx.doi.org/10.1524/zkri.2010.1210.

[4] H. Klein, Precession electron diffraction of Mn_2O_3 and $PbMnO_2$.75: solving structures where X-rays fail, Acta Crystallogr. Sect. A 67 (3) (2011) 303–309, http://dx.doi.org/10.1107/S0108767311009512.

[5] J.-L. Rouviere, A. Béché, Y. Martin, T. Denneulin, D. Cooper, Improved strain precision with high spatial resolution using nanobeam precession electron diffraction, Appl. Phys. Lett. 103 (24) (2013) 241913, http://dx.doi.org/10.1063/1.4829154.

[6] E.F. Rauch, J. Portillo, S. Nicolopoulos, D. Bultreys, S. Rouvimov, P. Moeck, Automated nanocrystal orientation and phase mapping in the transmission electron microscope on the basis of precession electron diffraction, Z. Kristallogr. 225 (2–3) (2010) 103–109, http://dx.doi.org/10.1524/zkri.2010.1205.

[7] D. Viladot, M. Véron, M. Gemmi, F. Peiró, J. Portillo, S. Estradé, J. Mendoza, N. Llorca-Isern, S. Nicolopoulos, Orientation and phase mapping in the transmission electron microscope using precession-assisted diffraction spot recognition: state-of-the-art results, J. Microsc. 252 (1) (2013) 23–34, http://dx.doi.org/10.1111/jmi.12065.

[8] A.S. Eggeman, J.S. Barnard, P.A. Midgley, Aberration-corrected and energy-filtered precession electron diffraction, Z. Kristallogr. Cryst. Mater 228 (1) (2013) 43–50, http://dx.doi.org/10.1524/zkri.2013.1565.

[9] T.A. White, A.S. Eggeman, P.A. Midgley, Is precession electron diffraction kinematical? Part I:: "phase-scrambling" multislice simulations, Ultramicroscopy 110 (7) (2010) 763–770, http://dx.doi.org/10.1016/j.ultramic.2009.10.013.

[10] A. Eggeman, T. White, P. Midgley, Is precession electron diffraction kinematical? Part II: A practical method to determine the optimum precession angle, Ultramicroscopy 110 (7) (2010) 771–777, http://dx.doi.org/10.1016/j.ultramic.2009.10.012.

[11] P.A. Midgley, A.S. Eggeman, Precession electron diffraction – a topical review, IUCrJ 2 (1) (2015) 126–136, http://dx.doi.org/10.1107/S2052252514022283.

[12] C.T. Koch, Aberration-compensated large-angle rocking-beam electron diffraction, Ultramicroscopy 111 (7) (2011) 828–840, http://dx.doi.org/10.1016/j.ultramic.2010.12.014, Special Issue: J. Spence's 65th birthday.

[13] J.S. Barnard, D.N. Johnstone, P.A. Midgley, High-resolution scanning precession electron diffraction: Alignment and spatial resolution, Ultramicroscopy 174 (2017) 79–88, http://dx.doi.org/10.1016/j.ultramic.2016.12.018.

[14] Y. Liao, L.D. Marks, On the alignment for precession electron diffraction, Ultramicroscopy 117 (2012) 1–6, http://dx.doi.org/10.1016/j.ultramic.2012.03.021.

[15] C. Ophus, Four-dimensional scanning transmission electron microscopy (4D-STEM): From scanning nanodiffraction to ptychography and beyond, Microsc. Microanal. 25 (3) (2019) 563–582, http://dx.doi.org/10.1017/S1431927619000497.

[16] J. Sunde, C. Marioara, A. van Helvoort, R. Holmestad, The evolution of precipitate crystal structures in an Al-Mg-Si(-Cu) alloy studied by a combined HAADF-STEM and SPED approach, Mater. Charact. 142 (2018) 458–469, http://dx.doi.org/10.1016/j.matchar.2018.05.031.

[17] H.W. Ånes, I.M. Andersen, A.T.J. van Helvoort, Crystal phase mapping by scanning precession electron diffraction and machine learning decomposition, Microsc. Microanal. S1 (2018) 586–587, http://dx.doi.org/10.1017/S1431927618003422.

[18] F. de la Peña, E. Prestat, V.T. Fauske, P. Burdet, T. Furnival, P. Jokubauskas, J. Lähnemann, M. Nord, T. Ostasevicius, K.E. MacArthur, et al., Hyperspy/hyperspy: Release v1.6.4, 2021, http://dx.doi.org/10.5281/zenodo.5082777.

[19] D.N. Johnstone, P. Crout, M. Nord, J. Laulainen, S. Høgås, E. Opheim, B. Martineau, C. Francis, T. Bergh, E. Prestat, et al., Pyxem/pyxem: pyxem 0.13.3, 2021, http://dx.doi.org/10.5281/zenodo.5075520.

[20] L. Jones, H. Yang, T.J. Pennycook, M.S.J. Marshall, S. Van Aert, N.D. Browning, M.R. Castell, P.D. Nellist, Smart Align—a new tool for robust non-rigid registration of scanning microscope data, Adv. Struct. Chem. Imaging 1 (2015) 8–23, http://dx.doi.org/10.1186/s40679-015-0008-4.